Sunlight penetration dominates the thermal regime and energetics of a shallow ice-covered lake in arid climate

Huang, Wenfeng

2022-05-10

The Cryosphere

Sunlight penetration dominates the thermal regime and energetics of a shallow ice-covered lake in arid climate

Wenfeng Huang[1,2], Wen Zhao[1], Cheng Zhang[1], Matti Leppäranta[3], Zhijun Li[4], Rui Li[1], and Zhanjun Lin[2]

[1]Key Laboratory of Subsurface Hydrology and Ecological Effects in Arid Region (the Ministry of Education),
Chang'an University, Xi'an, China
[2]State Key Laboratory of Frozen Soil Engineering, Northwest Institute of Eco-Environment and Resources,
Chinese Academy of Science, Lanzhou, China
[3]Institute of Atmospheric and Earth Sciences, University of Helsinki, Helsinki, Finland
[4]State Key Laboratory of Coastal and Offshore Engineering, Dalian University of Technology, Dalian, China

Correspondence: Wenfeng Huang (huangwenfeng@chd.edu.cn) and Zhijun Li (lizhijun@dlut.edu.cn)

Abstract. The Mongolian Plateau is characterized by cold and arid winters with very little precipitation (snowfall), strong solar insolation, and dry air, but little is known about the thermal regimes of the ice and ice-covered lakes and their response to the distinct weather and climate in this region. In a typical large, shallow lake, ice and snow processes (cover) and under-ice thermodynamics were monitored for four winters in 2015–2019. Heat transfer at the ice–water interface and lake heat budget were investigated. The results revealed that persistent bare ice of 35–50 cm thickness transmits 20 %–35 % of the incident solar radiation into the water below. This is a dominant source for under-ice energy flows and causes/maintains high water temperature (up to 6–8 °C) and high heat flux from water to ice (averages of 20–45 W m^{-2}) in mid-winter, as well as higher heat conduction in the ice interior during freezing. The heat balance shows that the transmitted radiation and the heat flux from water to ice are the dominant and highly correlated heat flows in the lake. Both bulk water temperature and temperature structure are sensitive to solar transmittance and occasional snow events. Under-ice convective mixing does not necessarily occur because of stratification of salinity in the water body. In particular, salt exclusion during freezing changes both the bulk salinity and the salinity profile, which plays a major role in the stability and mixing of the water column in this shallow lake.

1 Introduction

Lakes are important water resources and provide vital habitats for aquatic ecosystems. More than 55 % of the world's lakes are located between 40 and 80° N in the Northern Hemisphere (Verpoorter et al., 2014) and have the potential to freeze seasonally (Kirillin et al., 2012), especially in Arctic, boreal, and temperate climates and high mountain regions. Due to distinct properties of ice compared to water, seasonal formation and decay of ice cover have tremendous impacts on the lake water quality (Yang et al., 2016), physical and chemical conditions (Yang et al., 2021; Cavaliere and Baulch, 2018; Huang et al., 2019a), the aquatic ecosystem (Griffiths et al., 2017; Song et al., 2019), and land–atmosphere mass and heat interaction (Wang et al., 2015; Franz et al., 2018). Therefore, common concerns have been widely spread on mapping lake ice physics and its underlying physical mechanisms in the evolution of ice seasons.

Field and modeling investigations on lake ice processes have a long history in northern temperate and boreal regions, such as Fennoscandia, central Europe, northern Canada, and the Great Lakes. The shortening of ice cover period has been documented currently in lakes in these northern regions (Bernhardt et al., 2012; Lei et al., 2012; Karetnikov et al., 2017; Ptak et al., 2020). However, the lake ice regime has remained less studied due to lack of long-term observational records in arid climate regions, such as central Asia and high mountains, which are subject to a quite different landscape,

regional climate, and hydrological cycles compared with the northern temperate, boreal, and Arctic environments.

Lake thermal stratification is of great importance to hydrodynamics and transport of nutrients, oxygen, and primary production, which influence limnological habitats and ecosystems. In freezing freshwater lakes, stable inverse thermal stratification usually forms and persists under the ice cover with the temperature lower than the maximum density temperature (3.98 °C). After the onset of melting, strong solar irradiance can penetrate the ice cover into the water and drive turbulent convection (Bouffard et al., 2019; Volkov et al., 2019) until the bulk temperature reaches or surpasses the maximum density temperature or until breakup (Yang et al., 2020). However, in some shallow midlatitude brackish lakes, this is not the story. During the melting period, a warm middle layer may form due to salinity stratification and separate the overlying inverse thermal stratification and the underlying positive thermal stratification. The temperature of this warm layer can go up to around 10 °C before the breakup (e.g., Huang et al., 2019b; Kirillin et al., 2021). This underlines the uniqueness of seasonally ice-covered lakes in midlatitude arid regions and the importance of their different climate. It still remains unclear how this stratification forms and evolves and how it interacts with the snow–ice cover.

After freeze-up, the ice cover shelters the lake from atmospheric forcing and deposits. The lake boundary constitutes only the ice cover on the top and sediment at the bottom. The heat budget is governed by radiative and sensible fluxes across the ice–water–sediment interfaces (Leppäranta, et al., 2019). But these fluxes, including solar radiation transfer, ice–water heat exchange, and sediment heat release, have not been well quantified in midlatitude arid-region lakes. Especially the ice–water heat flux, a key factor affecting the mass and energy balance of both ice and water, has been demonstrated to be remarkably higher in Central Asia than in Arctic and boreal zones (Malm et al., 1997; Jakkila et al., 2009; Huang et al., 2019a, b; Lu et al., 2020). But the regime underpinning its high values is still unknown.

To fill the knowledge gaps in winter thermodynamics of lakes in cold and arid Asia and their background energy flows, we performed a four-winter observation program of snow–ice processes, solar radiation transfer, and temperature profiles of air–ice–water–sediment column in a typical large shallow lake that is seasonally ice-covered for 4–5 months, located on the southern border of the Mongolia Plateau. Below, observations and models are combined (1) to reveal the seasonal and diurnal dynamics of the temperature stratification under ice in the midlatitude arid climate, and (2) to quantify and balance the involved heat fluxes that determine the thermal state of the lake.

2 Data and methods

2.1 Study site

The Hetao Basin (ca. 6000 km^2, mean altitude > 1000 m), one of the oldest and largest irrigation areas in China, is located in the central southern Mongolian Plateau, controlled by a temperate continental climate. In the Hetao Basin, the annual sunshine duration is 3000–3200 h, the annual air temperature is 5.6–7.4 °C with the lowest and highest monthly temperatures of -14 to -11 °C (January) and 22 to 24 °C (July), the frost-free period is 130–150 d, and the annual precipitation is 150–400 mm concentrated in the warm season. Most parts of the basin have been desertified or semi-desertified in recent decades.

Lake Ulansuhai (40°36′–41°03′ N, 108°41′–108°57′ E; altitude 1019 m) is a typical large, shallow lake in a desert/semi-desert region with a total area of about 306 km^2 (Fig. 1). It is a very important part of the irrigation and drainage system of the Hetao Basin, and its major water source comes from the farmland irrigation drainage and domestic sewage. The maximum and mean depths are 2.5–3.0 and 1.0–1.5 m, respectively. The annual air temperature, hours of sunshine, precipitation, evaporation, wind speed, and frost-free period are 7.3 °C, 3185 h, 224 mm, 1502 mm, 3.5 m s^{-1}, and 152 d, respectively (Sun et al., 2011). The solar noon-time and altitude in winter are 12:45 $\pm$ 15 min and 41 $\pm$ 10°, respectively. The ice cover is usually free of snow or only sparsely snow-covered due to occasional snowfall events and strong winds.

The lake surface elevation is regulated through pumping water from the Yellow River via the main inflow canal at the western shore. The total annual water supply is approximately 4×10^8 m^3, equivalent to the lake volume. But in winter (November–March), very little surface inflow/outflow exists except possible minor wastewater inflow (Sun et al., 2013), and the subsurface inflow is also negligible (Zhu et al., 2014). For more detailed information, please consult Lu et al. (2020) and references therein.

According to our sampling tests in winter 2017, the lake water is brackish or weakly saline with a salinity of 1.0‰–1.5‰ before ice-on, gradually increasing to 2.5‰–3.0‰ due to exclusion of salts when the ice grows to its annual maximum.

Due to its unique climate and eutrophication, the lake ecology under the ice cover is very active with high rates of primary production and respiration. This is believed to be highly related to the under-ice solar irradiance and temperature and the key role of ice and snow processes (Song et al., 2019; Huang et al., 2021). Our previous observations revealed the mass and heat balance of the lake ice cover and the impacts of warm water under the ice cover (Lu et al., 2020), but further investigations were performed and combined here to look into the thermal stratification regimes.
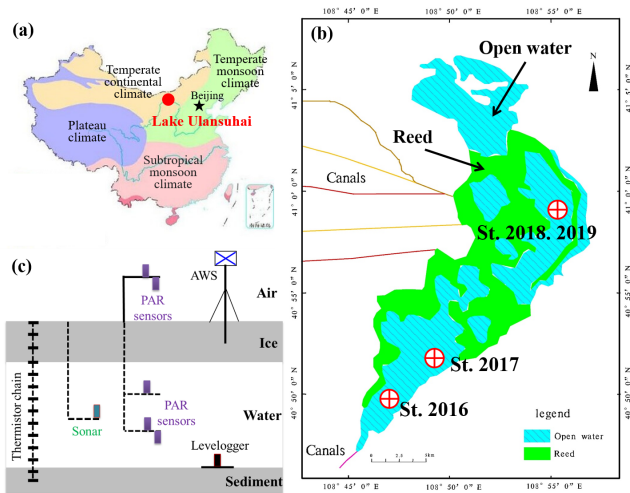
Figure 1. Locations of Lake Ulansuhai **(a)** and study sites **(b)** and the field instrumentation **(c)**. In each winter, a thermistor chain was refrozen into the ice cover to measure the temperature profile of the air–ice–water–sediment column with an established automatic weather station (AWS); more than three radiation sensors over the photosynthesis active radiation (PAR) band were deployed to observe the incident, reflected, and transmitted solar radiation.

2.2 Data acquisition

During winters of 2015–2019, field campaigns were conducted in open, reed-free areas of Lake Ulansuhai (Figs. 1c and 2). In each winter, an automatic weather station (AWS) was established on the ice cover to record wind speed and direction, air temperature and humidity, incident and reflected global radiation (300–3000 nm), and the temperature of the ice–snow surface. An under-ice up-looking sonar (WUUL-1/2, Wuhan University, China) was used to measure the ice thickness evolution with an accuracy of 2 mm. Snow thickness was measured manually using a snow stake every 1–2 d. The temperature profile of the air–ice–water–sediment column was observed using a thermistor chain (PTWD, Jinzhou Sunshine Technology Co. Ltd, China) at 5–10 cm spacing with an accuracy of 0.05 °C. TriOS spectral radiometers with an accuracy of 0.04–0.06 mW m^{-2} nm^{-1} (RAMSES-ACC-VIS, TriOS, German) were used to measure the incident and reflected photosynthetically active radiation (PAR) over the ice–snow surface and under the ice cover. The water level was monitored using a temperature–pressure logger with an accuracy of 0.05 % (LTC Levelogger, Solinst, Canada) placed 20 cm above the sediment surface. All the above variables were recorded every 10 min. Information on the acquired datasets is summarized in Table 1 (see also Huang et al., 2021).

In the winter of 2017, the under-ice water electric conductivity (EC) was measured using three online conductivity loggers (HOBO U24, Onset, USA, accuracy of 3 %) at depths of 60, 100, and 150 cm from 21 January to 11 March (Table 1).
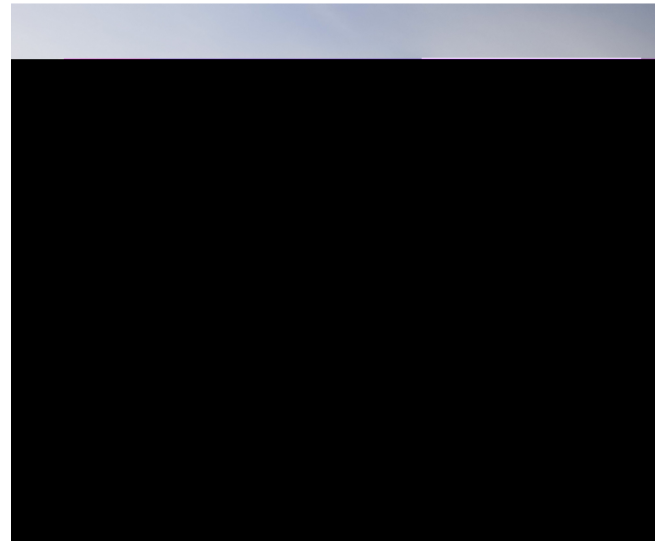

Figure 2. Field setup of apparatuses deployed and corresponding monitored variables in winter of 2019.

Concurrently, ice and water samples with 5 cm spacing were collected 8 times this winter to measure their EC and salinity using a portable YSI salinometer with an accuracy of 1 %.

2.3 Heat flux calculation and balance

In freshwater lakes, the water temperature is colder than 3.98 °C with a weak inverse thermal stratification during freezing (winter I stage), and typically a convective mixing layer forms between the top cold interfacial layer and the warm quiescent layer during melting (winter II stage) (Kirillin et al., 2012). The stratification structure in Lake Ulansuhai was checked using the temperature gradient following Kirillin et al. (2018).

After freeze-up, as illustrated in Fig. 3, the thermal regime of the water column is governed by the solar irradiance penetrating through the ice cover (R_w), solar radiation absorbed by the lake sediment (if any) (R_{sed}), heat fluxes through ice–water (F_w) and water–sediment (F_{sed}) interfaces, and horizontal heat gain by advection and diffusion (F_h) from the neighboring water body. If the zero-reference level for heat is defined as the heat content of liquid fresh water at its freezing-point temperature, the heat content of water is $\rho_w c_w T_w h_w$, and the heat budget of a water column is

$$R_w - R_{sed} + F_{sed} + F_h - F_w = \rho_w c_w h_w \frac{dT_w}{dt}$$
$$+ \rho_w c_w T_w \frac{dh_w}{dt}, \quad (1)$$

where ρ_w, c_w, and T_w are the density, specific heat, and bulk temperature of water, respectively. Other variables are defined in Fig. 3. The lateral heat transport F_h is negligible in this shallow lake with a flat bottom (Rizk et al., 2014; Kirillin et al., 2015). The two terms on the right-hand side are the heat

Table 1. Data series acquired during the four-winter observation program.

Winter	2016	2017	2018	2019
Available duration	11 Jan–9 Mar	21 Jan–11 Mar	9 Jan–25 Feb	20 Jan–27 Feb
Water depth	220 cm	170 cm	143 cm	140 cm
Ice–snow thickness	✓	✓	✓	✓
Air–ice–water–sediment temperature profile	5 cm spacing in ice, 10–15 cm spacing in water and sediment	5 cm spacing in ice, 5–10 cm spacing in water and sediment	5 cm spacing in ice, 5–10 cm spacing in water and sediment	5 cm spacing in ice, 10 cm spacing in water and sediment
Under-ice irradiation	175 cm	80, 130 cm	65, 90, 120 cm	80, 120 cm
Under-ice upwelling radiation		105 cm	100 cm	
Water level		✓		
Electric conductivity		60, 100, 150 cm		

Note: the observed depths for under-ice irradiation and upwelling radiation and electric conductivity denote the distances below the ice surface.

content changes induced by changes in the water temperature and depth, respectively. The water level logger indicated that the lake lost water through seepage to soil quite slowly (about $0.6\,\mathrm{mm\,d^{-1}}$) during ice seasons, and the heat loss due to the bottom water seepage was estimated to be smaller than $0.8\,\mathrm{W\,m^{-2}}$ and thus was ignored as a minor term compared to the other heat fluxes.

Under-ice solar irradiance

The light extinction coefficient of the under-ice water was measured as $2.1\,\mathrm{m^{-1}}$ under a clear sky on 7 January 2018. Using the observed irradiance by under-ice spectral sensors, the solar irradiance at the ice–water interface (R_w) was derived from a one-band exponential decay law of light transfer in the water column, following

$$R_\mathrm{w} = R_\mathrm{d}\exp(\kappa_\mathrm{w}(z_\mathrm{d} - h_\mathrm{i})), \tag{2}$$

where R_d is the observed downward irradiance at depth z_d, h_i is the ice thickness, and κ_w is the light extinction coefficient of water.

Sediment heat flux

The heat exchange flux through the water–sediment interface (F_sed) was calculated with the gradient method:

$$F_\mathrm{sed} = -\kappa_\mathrm{sed}\frac{\partial T_\mathrm{sed}}{\partial z}\bigg|_\mathrm{bottom} \approx -\kappa_\mathrm{sed}\frac{\Delta T_\mathrm{sed}}{\Delta z}, \tag{3}$$

where κ_sed is the thermal conductivity of sediment, and T_sed is the observed sediment temperature. In the winter of 2018, four thermistors were buried in the sediment (1, 9, 17, and 30 cm below the sediment surface) to measure the sediment temperature profiles. Assuming the heat transfer in the top

sediment is governed by the typical one-dimensional vertical heat conduction equation, we deployed an optimal control model to retrieve the effective thermal diffusivity of the sediment based on the observed sediment temperature profiles. For details on the optimal control model, please refer to Shi et al. (2014). The thermal conductivity can be determined ($0.2–0.7\,\mathrm{W\,m^{-1}\,^\circ C^{-1}}$) with the measured density and specific heat capacity of sediment. $\kappa_\mathrm{sed} = 0.5\,\mathrm{W\,m^{-1}\,^\circ C^{-1}}$ was used in Eq. (3).

Water-to-ice heat flux

The water-to-ice heat flux can be derived from the heat balance at the ice–water interface:

$$F_\mathrm{w} = Q_\mathrm{c} - Q_\mathrm{l} = -\kappa_\mathrm{i}\frac{\partial T_\mathrm{i}}{\partial z}\bigg|_{z=h_\mathrm{i}} - \rho_\mathrm{i}L_\mathrm{f}\frac{\partial h_\mathrm{i}}{\partial t}, \tag{4}$$

where Q_c and Q_l are the conductive heat flux to ice and the latent heat due to freezing/melting, respectively, and ρ_i and L_f are the density and latent heat of fusion of ice, respectively. The first term denotes the heat conduction into the ice interior, which can be derived using the temperature gradient in the bottom ice layer. The second term on the right-hand side denotes the heat release/absorption due to freezing/melting, which can be derived from ice thickness observations.

The heat content due to temperature change (i.e., the first term on the right-hand side of Eq. 1) was calculated using the observed water temperature profiles.

The direct use of semi-hourly observed datasets brought high-frequency fluctuations in estimated heat flux, and then daily means were used for further analysis of seasonal dynamics.

Figure 3. Heat budget components of the water column under the ice (modified from Huang et al., 2019b).

Table 2. Uncertainties in calculation of heat fluxes.

Error source	Errors in heat flux (W m^{-2})*			
	R_w	F_{sed}	F_w	$F_{Tw} = \rho_w c_w h_w \frac{dT_w}{dt}$
Radiation precision	0.08	–	–	–
Thermistor precision	–	0.25	1.1	1.7
Ice thickness	0.1	–	–	0.01
Ice growth rate	–	–	0.3	–
Ice density	–	–	1.25	–
Water density	–	–	–	0.2

* Dashes (–) indicate inapplicable.

2.4 Potential errors in heat flux estimation

Potential errors in the above heat flux estimation usually come from the measurement accuracy of the deployed apparatuses. The maximum error for each flux was determined based on the related apparatus accuracy (Table 2). The thermistor accuracy is expected to lead to errors of less than 1.7 W m^{-2} in F_s and F_{Tw}, and the ice density caused errors of less than 1.3 W m^{-2} in F_w. Other heat fluxes suffer only negligible uncertainties (< 0.3 W m^{-2}) induced by individual sources. Errors from several sources may accumulate especially in F_w, but the accumulated errors in F_w should be less than 8 %.

3 Results

3.1 Lake ice and temperature

Our observations were conducted during mid-winter covering the turning point from ice growth to melting. The air temperature was consistently lower than 0 °C, but its daily amplitude was very high (10–16 °C), and the peak at noon/afternoon could be close to 0 °C (Fig. 4). Wind speed was generally lower than 4 m s^{-1} except occasional gusts that led to snow or dust drifting. The relative humidity of air 2 m above the ice surface also showed an evident diurnal cycle between 40 % and 80 %.

The peak incident solar radiation was each day roughly 500–800 W m^{-2}, and its daily average was 80–200 W m^{-2}, showing an increasing trend from the beginning to the end of our observation period. But the daily average was always smaller than 100 W m^{-2} due to prevailing cloudy or overcast skies in winter 2019. Occasional snowfalls usually brought thin snow layers (< 6 cm) that continuously ablated due to blowing wind, melting, and sublimation. A new snow cover could increase the surface albedo up to over 0.80, but this increment gradually disappeared within 1 week following the snowfall.

The maximum annual ice thickness varied between 35 and 60 cm, accounting for 30 %–60 % of the mean lake depth. The bulk water temperature under the ice cover was 3–7 °C and showed diurnal cycles and synoptic decreases following snowfall events, evidencing the decrease in transmitted solar radiation. The sediment surface layer was always warmer than the water column during the observation period, showing that the sediment works as a heat source to the overlying water.

3.2 Thermal stratification and mixing in midwinter

In mid-winter, the lake sediment was still very warm with surface temperature > 6 °C, usually causing temperatures higher than 4 °C in the lower part of the water column (Fig. 5). It is hypothesized that this stratification was supported by salinity stratification. There is no detailed concurrent salinity profile data available, but the bulk salinity is of the order of 1 ‰, enriched in the ice season. As was observed in the winter of 2017 (Fig. 6), stable salinity stratification existed during the freezing period, and as salt was continuously excluded to water through the ice–water interface during water freezing, the bulk salinity increased, and the salinity structure gradually approached neutral stratification. But when the ice melting began on 7 March, the bulk salinity decreased, and stable salinity stratification formed again due to fresher meltwater intrusion. The sensitivity of density to temperature is very low in the neighborhood of 4 °C, so quite small salinity changes can compensate for the observed temperature structure for neutral density stratification. Although our observations did not cover the whole ice season, evident seasonal and annual variations were observed.

A common thin layer (10–30 cm) of strong inverse stratification (i.e., interface layer) prevailed just beneath the ice due to the large difference in temperature of the ice base at the freezing point and the bulk water column, e.g., in the winters of 2016, 2018, and 2019. But in winter 2017, this thin top layer did not show up, and a persistent thick inverse structure

Figure 4. Observational air temperature T_a **(a)**, daily means of incident and transmitted solar radiation **(b)**, snow and ice thickness **(c)**, temperature of the water column and surface sediment **(d)**. (Top left: winter 2016; top right: winter 2017; bottom left: winter 2018; bottom right: winter 2019.)

developed through the water column (Fig. 5b). Underneath the top cold interface layer, the temperature increased slowly downward to the warm sediment (weak inverse structure) in winter 2019 and prior to 3 March in winter 2016 (Fig. 5a and d). After 3 March in winter 2016 and 10 February in winter 2018, a thermally homogeneous convective layer quickly developed after the bulk water temperature rose above approximately 7 °C (Fig. 5a and c). Strikingly, before the formation of convective mixing in winter 2018, a "warm" zone of 30 cm (local maximum temperature) with temperature decreasing both downwardly and upwardly persisted at ~ 30 cm beneath the ice base. This abnormal layer is sometimes called a local temperature minimum (Mironov et al., 2002) or a "temperature dichotomy" (i.e., a dicothermal layer used in oceanography) (e.g., Kirillin and Terzhevik, 2011; Kirillin et al., 2021).

Water temperature contours (not shown) revealed that both the bulk temperature and thickness of the dicothermal layer show significant diurnal cycles: its temperature and thickness increase following the solar insolation cycle and decrease or even disappear during the night. The development and extension of this layer also increase the thermal gradient of the overlying interface layer.

Occasional snowfall events usually led to quick bulk cooling along the entire water temperature profile due to the high reflection of new snow despite their small thickness. The sensitive response of water temperature to snow events (actually changes in penetrated radiation) implies large heat flux from water to ice and the dominance of solar radiation in this lake.

Unconventionally, under-ice convection did not take place in all winters (only two of our four observational winters)
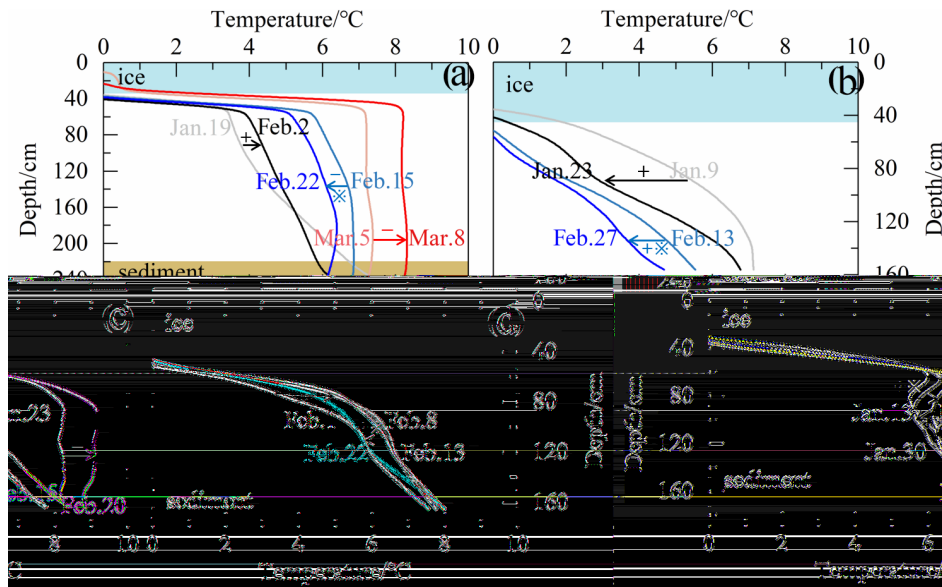
Figure 5. Daily profile evolution of the water column during ice season of the winters of **(a)** 2016, **(b)** 2017, **(c)** 2018, and **(d)** 2019. Light blue and brown zones denote ice cover and bottom sediment, respectively. Asterisks (∗) denote snowfalls and snow-covered periods. Plus (+) and minus (−) denote the growth and melt stage of the ice cover.

and seems to develop just when the bulk water temperature goes up to 7 °C. This temperature threshold is higher than the temperature of maximum density of freshwater (3.98 °C) and saline water (< 3.98 °C). These annually variable convections are believed to form conditionally and lake-specifically with the proper water–sediment temperature and salinity profile. When the water temperature is high enough, its density effect overcomes salinity stratification, and convection is thus triggered. Taking the winter of 2017 as an example, water sampling indicated that, in this very shallow lake, the salinity increased, and its profile structure changed simultaneously as the ice grew (Fig. 6). At ice-on, the salinity showed a stable profile (increasing downwardly), and its impact on water density outweighed the impact of concurrent temperature gradient (i.e., on 5 January). With the following ice growth, the bulk salinity increased, but the salinity gradient decreased, and the temperature gradient decreased. Consequently, the weakened salinity gradient could persistently outweigh or offset the impact of the temperature profile on water density through the growing period (before 4 March). Otherwise, if the weakening gradient of salinity no longer offsets the temperature effect, the convective mixing takes place across the density instability layer. This is very likely why under-ice mixing occurred in the winters of 2016 and 2018. When the ice started melting, fresh meltwater intrusion from the top increased the salinity gradient and thus kept the water column more stable again (on 11 March).

We can conclude that how the water temperature and salinity profiles change synchronously during late freezing and initial melting determines whether the under-ice convection takes place. Especially if the sediment temperature is high

and the transmitted radiation is large during freezing, the sediment and bottom water temperature can be warm and increase rapidly, increasing the probability for full-depth convection such as in the winters of 2016 and 2018.

3.3 Heat transfer at the ice–water interface

Heat and mass fluxes at the ice–water interface govern the basal freezing/melting rate of ice cover and the temperature of the top water layer. Our data show that in mid-winter, ice growth slowed down, and then a near-equilibrium period appeared (i.e., the thickness kept roughly constant) prior to the start of the melting period (Fig. 4). At the ice bottom, the latent heat flux Q_1 stayed positive during continuous ice growth and fluctuated near the zero level during the near-equilibrium period. Thereafter the ice began to melt from the bottom, and Q_1 turned negative (Fig. 7). The conductive heat flux Q_c through the bottom ice layer remained positive, indicating upward heat transport. After the ice had started fast melting, Q_c went down to near zero with the ice cover turning into a (quasi-)isothermal state.

The water-to-ice heat flux F_w showed a similar variation to Q_c. Physically, F_w is crucially determined by the inverse thermal gradient of the topmost interface layer. The thinner interface layer with the higher thermal gradient in the winters of 2016 (temporal average ± standard deviation: $40.8 \pm 11.7 \, \text{W m}^{-2}$) and 2018 ($44.9 \pm 9.4 \, \text{W m}^{-2}$) created higher F_w than those in the winters of 2017 ($21.4 \pm 12.3 \, \text{W m}^{-2}$) and 2019 ($30.2 \pm 9.0 \, \text{W m}^{-2}$). Interestingly, the convective mixing process increased F_w by 33 % in winter 2016 but decreased F_w by 26 % in winter 2018 com-
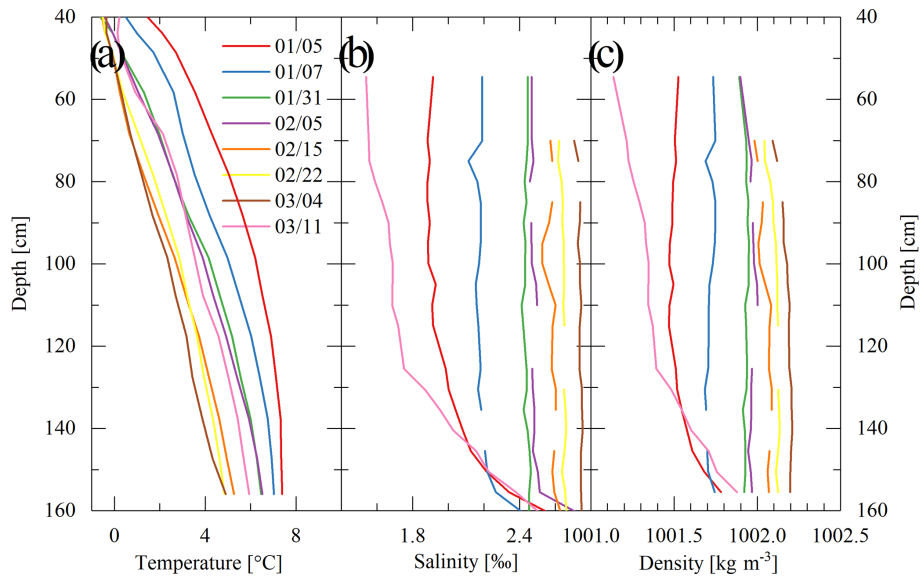
Figure 6. Observed temperature and salinity profiles and estimated water density (according to Leppäranta, 2015) in winter 2017.

pared with F_w before the convection occurrence, indicating complicated effects of convection.

During the ice growth, both latent heat due to freezing (Q_l) and conductive heat from water to ice (F_w) need to be taken out by the ice conduction heat (Q_c) (Eq. 4). Q_c was predominantly determined by the ice thickness and surface heat balance (Leppäranta, 2015), so a higher F_w meant lower Q_l and growth rate of ice. Specifically, F_w took up > 65 % of Q_c prior to the equilibrium stage (e.g., winters of 2016 and 2017) and > 90 % in the equilibrium stage (e.g., winters of 2018 and 2019); the remaining Q_c was used to take the latent heat of freezing out to the atmosphere through the ice cover, leading to continuous ice growth.

During initial ice melting, the heat transfer from water to ice (F_w) was largely conducted through the ice cover (Q_c) (70 %–80 %) and partly used to melt the basal ice (Q_l). But during the following fast melting, Q_c was negligible since the isothermal ice cover depressed or even prevented heat conduction, and F_w was almost totally used for basal ice melt.

3.4 Energetics of the water column

The temperature regime of under-ice water is governed by the heat budget. Figure 8 shows all the heat fluxes involved and the balance residual. In mid-winter, the solar flux R_w was 25–50 W m^{-2} under bare ice cover and dropped to 1.5–13 W m^{-2} under ice with a snow cover of varying thickness (1.5–8 cm) and age. Only 3 %–14 % (1–5 W m^{-2}) of R_w (i.e., R_{sed}) reached the sediment surface (Fig. 4), which in turn released heat (F_{sed}) to the overlying water in mid-winter (1–3 W m^{-2}). The heat flux from water to ice, F_w, also showed interannual and seasonal variations (10–60 W m^{-2})

and was generally smaller under snow-covered ice than under bare ice, likely indicating the effect of transmitted sunlight. The heat content change (F_{Tw}) of water, as a resultant heat change from heat sources and sinks, was typically small (-5 to $+4$ W m^{-2}) during freezing but grew to 4–15 W m^{-2} during the initial melt.

Evidently, the transmitted solar radiation (R_w) and water-to-ice heat transfer (F_w) dominated the heat balance of the under-ice water. Combining the four-winter observations, R_w was the largest heat source (34.8 ± 18 W m^{-2}) and accounted for (92 ± 9) % of the total source ($R_w + F_{sed}$) to the under-ice water, while F_w was the largest heat sink (34.3 ± 15 W m^{-2}) and accounted for (96 ± 38) % of the total sink ($F_w + R_{sed}$). The term ($F_{sed} - R_{sed}$) was only -0.8 ± 2.7 W m^{-2}, and F_{Tw} was 0.7 ± 8.7 W m^{-2}, both of which can be neglected compared to others. Therefore, the transmitted solar radiation was almost totally (97 %) returned to the ice base by means of water-to-ice heat conduction.

Interannual comparisons indicated that winter 2017 with only a prevailing inverse temperature structure and a decreasing bulk temperature was different from other winters (Figs. 4 and 5). Heat flows and budget can provide basic insights into the differences. During the freezing period of winter 2017, the bulk water temperature kept decreasing because the net heat gain of water was negative (i.e., $R_w + F_{sed} - F_w < 0$); continuous heat loss of water to the ice bottom also created an inverse thermal gradient, and a decrease in water temperature prevented the occurrence of mixing. However, in other winters (especially 2016 and 2018), the net heat gain of water was positive, so the water temperature had an increasing trend, which increases the potential for mixing to occur. Compared with other winters, snow bands and spots that prevailed on top of a thicker ice cover in winter 2017
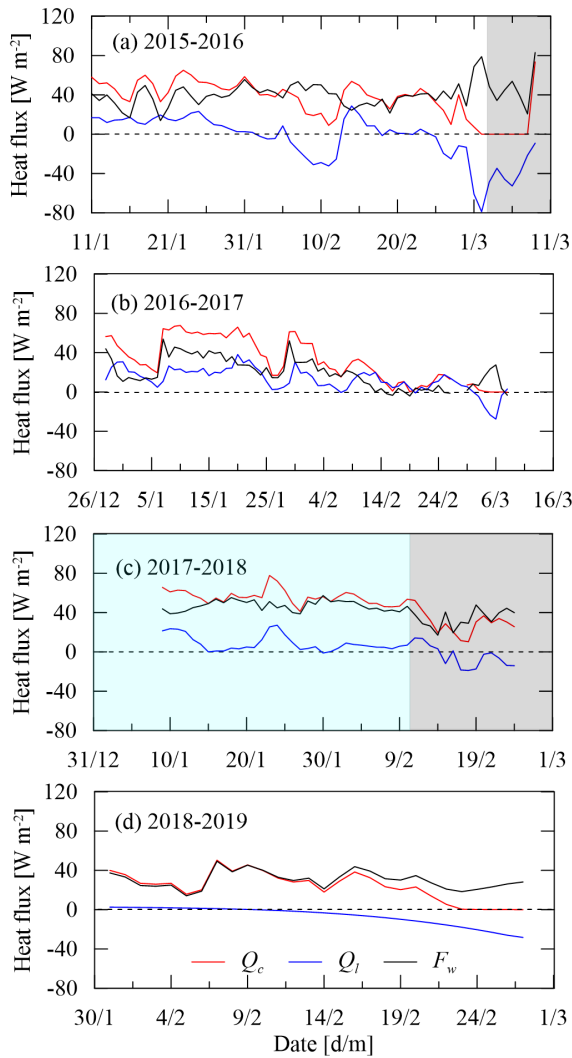
Figure 7. Heat fluxes at the ice–water interface (Q_c: conductive heat flux in the bottom ice; Q_l: latent heat flux due to basal ice freezing/melting; F_w: water-to-ice heat flux). The light gray and blue zones denote periods of convective mixing and stratification with the local "warm" layer (Fig. 5), respectively.
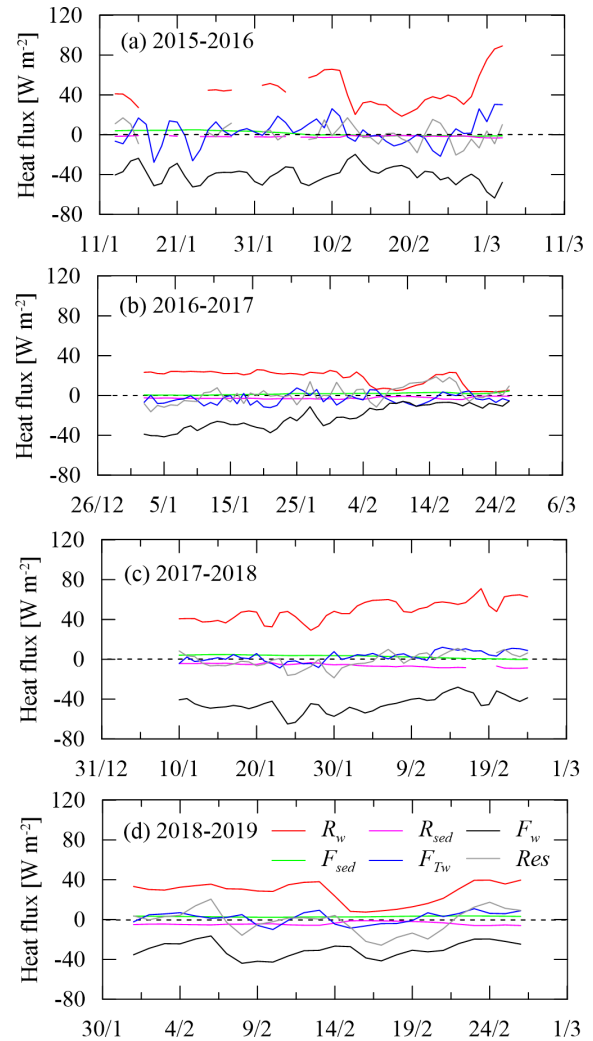
Figure 8. Heat budget of the under-ice water (R_w: transmitted solar radiation; R_{sed}: absorbed solar radiation by sediment; F_w: water-to-ice heat flux; F_{sed}: heat released from sediment; F_{Tw}: sensible heat caused by water heat content change; Res: residual of heat balancing, which is supposed to be zero when all heat fluxes balance ideally).

caused lower penetrated solar radiation, largely contributing to the general cooling of the water column.

4 Discussion

4.1 Comparisons with (sub-)Arctic and temperate climate lakes

Prior to the ice-on date, in freshwater lakes fall mixing due to thermally free convection (at 3.98 °C) and continuous wind stirring against weak salinity gradients usually creates a large/full-depth vertical isothermal structure with temperature quite close to the freezing point (stage I in Fig. 9).

After the freeze-up or ice-on, the under-ice stratification evolves as a joint result of snow and ice condition, solar radiation penetration into water, heat flux from the bottom sediment, and horizontal advection and diffusion. In Arctic, boreal, and northern temperate regions, such as Fennoscandia, north America, and central Europe, winter precipitation leads to thick snow cover on lake ice, and only a little sunlight can penetrate through the snow and ice cover and can thus be neglected in the water column. The water column receives heat from the bottom sediment and releases heat to the ice cover on top. These heat fluxes are small (0–5 W m^{-2}), and therefore the lake water stays close to the freezing point in the top layer and has a very weak inverse structure (curve I) through the entire growth period of 3–5 months. After the melting on-

set, warm air and strengthened solar radiation lead to snow melting, and more solar radiation goes through the transparent ice and heats up the underlying water, creating a deepening convective mixing (stage II) before reaching the temperature of maximum density (T_m) (stage III). Usually, the ice cover breaks up before the thermal state of stage III forms in most deep boreal and Arctic lakes (Yang et al., 2020).

In midlatitude cold and arid regions, intensive solar radiation and thin snow cover allow more solar energy transmittance to the water column just following the freeze-up. On the Qinghai–Tibet Plateau (QTP), the water column can keep a stable state of stage I or start slowly warming (i.e., period of stage II) just following the freeze-up in deep lakes and then go to stage III, creating mid-winter overturn (Fig. 9b). Afterwards, strong solar radiation due to thin ice warms continuously the top water layer (stage IV), which exists for 4–6 weeks before breakup (Kirillin et al., 2021; Lazhu et al., 2021). However, in shallow ponds, stage II (i.e., transition from stage I to III) is very short (1 week), and the water column roughly stays at stage III almost over the entire freezing period. The following warm layer (IV) can deepen to near the lake bottom before ice-off (Fig. 9c) (Huang et al., 2019b).

Lake Ulansuhai is very shallow and weakly saline, and although the solar radiation is strong, the thermal stratification dynamics is determined by the synchronous profile evolution of temperature and salinity. Although our observations covered only the mid-winter, the thermal profile of type I is expected at pre-winter and ice-on due to the joint effects of wind-stirring and salinity gradient. But stage I should be very short, and the bulk temperature increases rapidly, and the transition to stage II takes place due to the solar radiation transmittance and shallow lake depth. However, the occurrence of convective mixing (we used stage IIIb here for brackish water) is conditional and mainly dependent upon the salinity evolution due to the freezing exclusion effect. Stage IV is also expected since meltwater dilution in the top layer can suppress the convection. Note that the forming regime of stage IIIb is different in this brackish lake compared with stage III in freshwater lakes, which are predominantly driven by temperature approaching T_m with solar heating. In brackish lakes, convective mixing may be stopped by a dicothermal layer in the middle (Fig. 5c), and full convection is possible only when the bottom water is warm enough to conquer the salt stratification.

Salinity structure plays a more important role in lake stratification and convective mixing than the temperature in brackish/saline and even freshwater lakes with salinity below 0.5 ppt (parts per thousand; Kirillin and Terzhevik, 2011). The present results indicated that the salt exclusion during freezing changes both the total salt content and salinity structure. For instance, for a lake with a mean depth of 1.0 m, if the salinity segregation coefficient is assumed to be 0.15 (Pieters and Lawrence, 2009; Bluteau et al., 2017), the formation of a 0.5 m ice cover can cause an increment of 70 % to the water salinity. In Lake Ulansuhai, the salinity increases downward at ice-on with a large salinity gradient. Afterwards, as the ice grows, salt exclusion gradually decreases the salinity gradient, making the water more prone to mix convectively.

4.2   What leads to high water-to-ice heat flux?

The water-to-ice heat flux F_w plays a predominant role in the basal growth and melting of lake ice cover but is quite challenging to observe instrumentally. Equations (1) and (4) provide two ways to estimate F_w indirectly if the ice thickness, temperature profile of the ice–water–sediment column, and solar irradiance are observed (actually these variables were often observed in lake thermal regime and ice programs).

By definition, F_w is the conductive heat flux across the very thin diffusive water layer just beneath the ice. The temperature gradient and thickness of this thin layer are influenced to a varied extent by thermal stratification, convective mixing (Figs. 5 and 6), advection (Rizk et al., 2014; Kirillin et al., 2015), and seiche oscillation (Kirillin et al., 2018). All these thermal and hydraulic processes lead to non-stationary and spatiotemporally varying F_w (Winters et al., 2019).

In freshwater lakes, under-ice convective mixing is observed to increase heat transport to the ice bottom by increasing the thermal gradient of the interfacial layer above the convective layer (Mironov et al., 2002; Kirillin et al., 2018). However, in weakly saline Lake Ulansuhai, under-ice convective mixing does not necessarily take place every winter, and its impact on heat transport to the ice bottom differs between winters. For instance, in the winter of 2016, the convective mixing developed evenly across the entire water column and then encroached the overlying interfacial diffusive layer and increased the bottom temperature of this layer (Fig. 5a), resulting in an increase in the thermal gradient of this layer and thus enhancing the heat diffusion (i.e., increasing F_w). However, in the winter of 2018, the convection took place only in the lower half of the water column, slightly decreased the thermal gradient of the overlying diffusive layer, and eliminated the dicothermal layer that maintained relatively high F_w prior to the convection onset (Fig. 5c), leading to a decrease in F_w. In the future, detailed synchronous datasets on synchronous temperature and salinity profiles are needed to understand the accurate regime of convection in this type of lake.

Although we did not acquire concurrent salinity profiles to the water temperature, sampling results in the winter of 2017 inevitably indicate the development of double diffusion as the temperature destabilizes while the salinity stabilizes the stratification (Schmitt, 1994; Schmid et al., 2010). The effective heat diffusivity of the bulk water column estimated from F_w derived by Eq. (4) was 5–16 (mean of approximately 10) times larger than the molecular diffusivity, indicating the significantly enhanced diffusivity of heat due to the double diffusion.

In boreal and Arctic lakes, weak solar radiation, short insolation duration, and most importantly thick snow cover limit
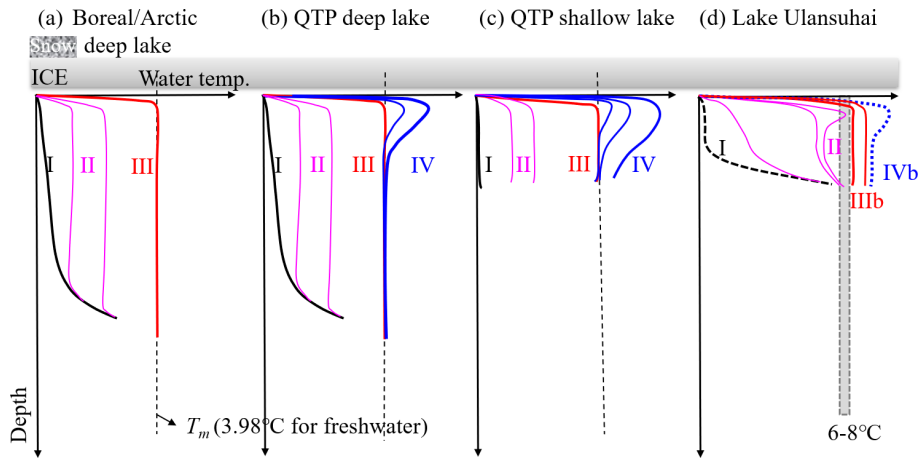
Figure 9. Typical thermal stratification types in ice-covered lakes: **(a)** deep lakes in the Arctic (Jakkila et al., 2009), **(b)** deep lakes on the QTP (Kirillin et al., 2021; Lazhu et al., 2021), **(c)** a shallow pond on the QTP (Huang et al., 2019b), and **(d)** Lake Ulansuhai. The definitions of Roman numerals are presented in the text.

solar heat input to the under-ice water column; just water and sediment heat release (both very small) can cause only low seasonal values, $F_w < 15 \, \mathrm{W \, m^{-2}}$ (Malm et al., 1997; Jakkila et al., 2009). However, in arid or midlatitude lakes with thin snow and/or more intensive solar insolation, F_w can be high, 10–50 $\mathrm{W \, m^{-2}}$ in Lake Baikal (Aslamov et al., 2017) and 20–100 $\mathrm{W \, m^{-2}}$ in QTP lakes with distinct seasonal variation (Huang et al., 2019a, b; Kirillin et al., 2021). The estimated F_w in Lake Ulansuhai is comparable to Lake Baikal and QTP lakes, indicative of the vital contribution of solar radiation and the absence of snow cover.

Higher F_w does not necessarily mean shorter freezing duration, thinner lake ice cover, or that growth is suspended. In Lake Ulansuhai, in ice growth, the conductive heat in the ice cover (Q_c) is much higher, which means that the F_w can be totally released through the ice cover, and the freezing latent heat (Q_l) can also be taken out since $F_w + Q_l = Q_c$. This ensures the continuous growth of ice. In ice melting, the Q_c can usually be ignored; the under-ice water supplies heat (F_w) to maintain basal ice melting (Q_l). Higher F_w means a greater melting rate.

From a perspective of heat balance in water (Eq. 1),

$$F_w = R_w - R_{sed} + F_{sed} + F_h - \rho_w c_w h_w \frac{dT_w}{dt}$$
$$- \rho_w c_w T_w \frac{dh_w}{dt}. \tag{5}$$

If we define $Q_{rad} = R_w - R_{sed}$ (i.e., solar absorption by the water column) and if the heat content change due to subsurface water seepage is negligible, Eq. (5) is transformed to

$$F_w = Q_{rad} + F_{sed} + F_h - F_{Tw}, \tag{6}$$

which means the solar energy (Q_{rad}) and sediment heat (F_{sed}) are used to change the bulk water temperature (F_{Tw})

and its structure. In turn, the water body loses heat to the ice by adjusting its bulk temperature and structure. R_{sed} is usually very small, so

$$Q_{rad} \approx R_w. \tag{7}$$

Eq. (6) can be transformed to a simple linear formula to present the contribution of R_w:

$$F_w = a R_w + b, \tag{8}$$

where slope a reflects the contribution of the penetrated solar radiation, while intercept b reflects the integrated contributions of other heats. Figure 8 argued that both F_{sed} and F_{Tw} are very small and roughly constant, and R_w and F_w are the overwhelming dominant heat source and sink, respectively. In consequence, if we fit the $F_w \sim R_w$ data using $a = 1$, the regressed mean contribution of heat fluxes is $-3.1 \, \mathrm{W \, m^{-2}}$ (red line in Fig. 10), very close to the estimate of $-1.5 \, \mathrm{W \, m^{-2}}$ in Sect. 3.4. If we ignore the minor intercept, the line with $a = 0.93$ explains approximately the same amount of variance in the observations (blue line in Fig. 10), consistent with the observed ratio of F_w to R_w (0.97).

We have to note that values of both coefficients should be lake-specific. Lake depth and salinity modify the changes in convective mixing depth, bulk water temperature, and temperature structure caused by solar irradiance (Lazhu et al., 2021), and they thus alter the relative contributions of solar radiation to water heat content and to heat transfer from water to ice. For instance, in a deep lake with a mean depth of 20 m in Finland, one-third of the transmitted solar radiation returned to ice (Leppäranta et al., 2019).

5 Conclusions

We present the ice-covered lake thermodynamics in a midlatitude, cold, and dry region where the climatic and hydrolog-
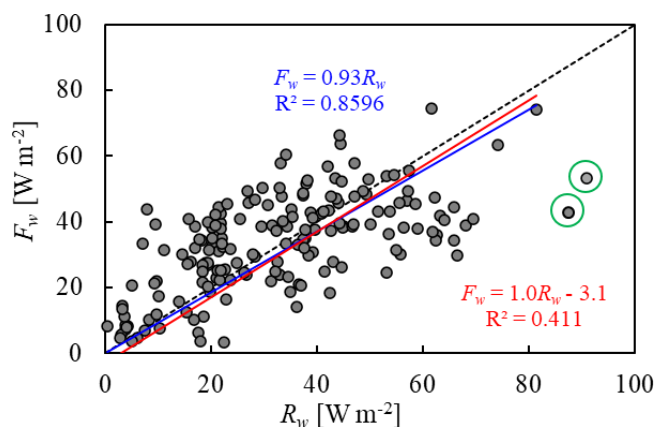
Figure 10. Linear fitting of daily water-to-ice heat flux F_w as a function of penetrated solar radiation R_w. The dashed black line denotes $F_w = R_w$. Two models were used to fit the data with two dots in green circles being removed.

ical environment is in distinct contrast to the Arctic, boreal, and other northern temperate regions. The ice cover is always bare or covered by only occasional thin snow patches lasting for 1–2 weeks due to the arid climate and blowing wind. The clear congelation ice cover allows one-fifth to one-third of incident solar radiation to penetrate into the water column in mid-winter, providing a background for the energetics of under-ice water. The transmitted radiation and heat transfer across the ice–water interface dominate the heat budget of the water column and are highly correlated. High water-to-ice heat flux F_w (daily averages of 20–45 W m^{-2}) was observed compared to that in (sub-)Arctic and boreal lakes and takes up > 90 % of the solar radiation input to the under-ice water (20–50 W m^{-2}). Snow accumulations can decrease F_w due to its large albedo and light attenuation. Despite high F_w, higher heat conduction within the ice cover (30–55 W m^{-2}) existed during the freezing period because of the persistent snow-free ice surface and created continuous basal growth of ice. In particular, the high correlation between F_w and penetrating solar radiation indicates the temporal variation in F_w, which is important for updating F_w parameterization in lake ice modeling.

Both bulk water temperature and its structure show diurnal, synoptical, and seasonal variations due to their quick responses to transmitted radiation and snow events because of the shallow lake depth. Double diffusion should surely prevail in wintertime in this shallow saline lake and strengthen the heat transport to the ice bottom because there is always cooler and fresher water overlying warmer and saltier water. Under-ice convective mixing and/or dicothermal water layer mixing take place in some winters depending on the dynamic interaction between radiation (temperature) and salinity stratifications, which is mediated by the salt exclusion during freezing. However, details in double diffusion, convective mixing, and the effect of salt exclusion (or cry-

oconcentration) on water stratification in shallow ice-covered saline lakes need to be investigated in the future using high-frequency and high-resolution measurements.

Author contributions. WH, ML, and ZhiL conceived the study. WZ, HY, and ZhanL conducted the field observations. WZ, CZ, RL, and ZhiL analyzed data on meteorology and ice–snow conditions. WH and ML developed and ran the model. WZ, RL, and WH calculated the heat budgets for the water column. WH and WZ wrote the paper with contributions from all the co-authors.

References

Aslamov, I. A., Kozlov, V. V., Kirillin, G. B., Mizandrontsev, I. B., Kucher, K. M., Makarov, M. M., and Granin, N. G.: A study of heat transport at the ice base and structure of the under-ice water layer in southern Baikal, Water Resour., 44, 428–441, 2017.

Bernhardt, J., Engelhardt, C., Kirillin, G., and Matschullat, J.: Lake ice phenology in Berlin-Brandenburg from 1947–2007: observations and model hindcasts, Climatic Change, 112, 791–817, 2012.

Bluteau, C. E., Pieters, R., and Lawrence, G. A.: The effects of salt exclusion during ice formation on circulation in lakes, Environ. Fluid Mech., 17, 579–590, 2017.

Bouffard, D., Zdorovennova, G., Bogdanov, S., Efremova, T., Lavanchy, L., Palshin, N., Terzhevik, A., Vinnå, L. R., Volkov, S., Wüest, A., Zdorovennov, R., and Ulloa, H. N.: Under-ice convection dynamics in a boreal lake, Inland Waters, 9, 142–161, https://doi.org/10.1080/20442041.2018.1533356, 2019.

Cavaliere, E. and Baulch, H. M.: Denitrification under lake ice, Biogeochemistry, 137, 285–295, 2018.

Franz, D., Mammarella, I., Boike, J., Kirillin, G., Vesala, T., Bornemann, N., Larmanou, E., Lang, M., and Sachs, T.: Lake-atmosphere heat flux dynamics of a thermokarst lake in arctic Siberia, J. Geophys. Res.-Atmos., 123, 5222–5239, https://doi.org/10.1029/2017JD027751, 2018.

Griffiths, K., Michelutti, N., Sugar, M., Douglas, M. S. V., and Smol, J. P.: Ice-cover is the principal driver of ecological change in High Arctic lakes and ponds, PLoS ONE, 12, e0172989, https://doi.org/10.1371/journal.pone.0172989, 2017.

Huang, W., Cheng, B., Zhang, J., Zhang, Z., Vihma, T., Li, Z., and Niu, F.: Modeling experiments on seasonal lake ice mass and energy balance in the Qinghai–Tibet Plateau: a case study, Hydrol. Earth Syst. Sci., 23, 2173–2186, https://doi.org/10.5194/hess-23-2173-2019, 2019a.

Huang, W., Zhang, J., Leppäranta, M., Li, Z., Cheng, B., and Lin, Z.: Thermal structure and water-ice heat transfer in a shallow ice-covered thermokarst lake in central Qinghai-Tibet Plateau, J. Hydrol., 578, 124122, https://doi.org/10.1019/j.jhydrol.2019.124122, 2019b.

Huang, W., Li, Z., Arvola, L., and Song, S.: DOT, radiation and ice/snow datasets in winter Lake Ulansuhai, Zenodo [data set], https://doi.org/10.5281/zenodo.4291840, 2020.

Huang, W., Zhang, Z., Li, Z., Leppäranta, M., Arvola, A., Song, S., Huotari, J., and Lin, Z.: Under-ice dissolved oxygen and metabolism dynamics in a shallow lake: The critical role of ice and snow, Water Resour. Res., 57, e2020WR027990, https://doi.org/10.1029/2020WR027990, 2021.

Jakkila, J., Leppäranta, M., Kawamura, T., Shirasawa, K., Salonen, K.: Radiation transfer and heat budget during the ice season in Lake Pääjärvi, Finland, Aquat. Ecol., 43, 681–692, 2009.

Karetnikov, S., Leppäranta, M., and Montonen, A.: A time series of over 100 years of ice seasons on Lake Ladoga, J. Great Lakes Res., 43, 979–988, 2017.

Kirillin, G. and Terzhevik, A.: Thermal instability in freshwater lakes under ice: Effect of salt gradients or solar radiation?, Cold Reg. Sci. Technol. 65, 184–190, 2011.

Kirillin, G., Aslamov, I., Leppäranta, M., and Lindgren, E.: Turbulent mixing and heat fluxes under lake ice: the role of seiche oscillations, Hydrol. Earth Syst. Sci., 22, 6493–6504, https://doi.org/10.5194/hess-22-6493-2018, 2018.

Kirillin, G., Leppäranta, M., Terzhevik, A., Granin, N., Bernhardt, J., Engelhardt, C., Efremova, T., Golosov, S., Palshin, N., Sherstyankin, P., Zdorovennova, G., and Zdorovennov, R.: Physics of seasonally ice-covered lakes: a review, Aquat. Sci., 74, 659–682, 2012.

Kirillin, G., Shatwell, T., and Wen, L.: Ice-covered lakes of Tibetan plateau as solar heat collectors, Geophys, Res. Lett., 48, e2021GL093429, https://doi.org/10.1029/2021GL0, 2021.

Kirillin, G. B., Forrest, A. L. Graves, K. E., Fischer, A., Engelhardt, C., and Laval, B. E.: Axisymmetric circulation driven by marginal heating in ice-covered lakes, Geophys. Res. Lett., 42, 2893–2900, 2015.

Lazhu, Yang, K., Hou, J., Wang, J., Lei, Y., Zhu, L., Chen, Y., Wang, M., and He, X.: A new finding on the prevalence of rapid water warming during lake ice melting on the Tibetan Plateau, Sci. Bull., 66, 2358–2361, https://doi.org/10.1016/j.scib.2021.07.022, 2021.

Lei, R., Leppäranta, M., Cheng, B., Heil, P., and Li, Z.: Changes in ice-season characteristics of a European Arctic lake from 1964 to 2008, Climatic Change, 115, 725–739, 2012.

Leppäranta, M.: Freezing of lakes and the evolution of their ice cover, Springer, Berlin, Heidelberg, https://doi.org/10.1007/978-3-642-29081-7, 2015.

Leppäranta, M., Lindgren, E., Wen, L., and Kirillin, G.: Ice cover decay and heat balance in Lake Kilpisjärvi in Arctic tundra, J. Limnol., 78, 163–175, https://doi.org/10.4081/jlimnol.2019.1879, 2019.

Lu, P., Cao, X., Li, G., Huang, W., Leppäranta, M., Arvola, L., Huotari, J., and Li, Z.: Mass and heat balance of a lake ice cover in the central Asian arid climate zone, Water, 12, 2888, https://doi.org/10.3390/w12102888, 2020.

Malm, J., Terzhevik, A., Bengtsson, L., Bovarinov, P., Glinsky, A., Palshin, N., and Petrov, M.: Temperature and salt content regimes in three shallow ice-covered lakes 2. Heat and mass fluxes, Hydrol. Res., 28, 129–152, 1997.

Mironov, D., Terzhevik, A., Kirillin, G., Jonas, T., Malm, J., Farmer, D.: Radiatively-driven convection in ice-covered lakes: Observations, scaling and mixed-layer model, J. Geophys. Res., 107, 3032, https://doi.org/10.1029/2001JC000892, 2002.

Pieters, R. and Lawrence, G. A.: Effect of salt exclusion from lake ice on seasonal circulation, Limnol. Oceanogr., 54, 401–412, 2009.

Ptak, M., Sojka, M., and Nowak, B.: Effect of climate warming on a change in the thermal and ice conditions in the largest lake in Poland-Lake Śniardwy, J. Hydrol. Hydromech., 68, 260–270, 2020.

Rizk, W., Kirillin, G., and Leppäranta, M.: Basin-scale circulation and heat fluxes in ice-covered lakes, Limnol. Oceanol., 59, 445–464, 2014.

Schmid, M., Busbridge, M., and Wüest, A.: Double-diffusive convection in Lake Kivu, Limnol. Oceanogr., 55, 225–238, 2010.

Schmitt, R. W.: Double diffusion in oceanography, Ann. Rev. Fluid Mech., 26, 255–285, 1994.

Shi, L., Li, Z., Niu, F., Huang, W., Lu, P., Feng, E., Han, H.: Thermal diffusivity of thermokarst lake ice in Beiluhe basin of the Qinghai-Tibet Plateau, Ann. Glaciol., 55, 153–158, 2014.

Song, S., Li, C., Shi, X., Zhao, S., Tian, W., Li, Z., Bai, Y., Cao, X., Wang, Q., Huotari, J., Tulonen, T., Uusheimo, S., Leppäranta, M., Loehr, J., and Arvola, L.: Under-ice metabolism in a shallow

lake in a cold and arid climate, Freshwater Biol., 64, 1710–1720, https://doi.org/10.1111/fwb.13363, 2019.

Sun, B., Li, C. Y., and Zhu, D. N.: Changes of Ulansuhai Lake in past 150 years based on 3S technology, 2011 International Conference on Remote Sensing, Environment and Transportation Engineering, 2993–2997, https://doi.org/10.1109/rsete.2011.5964944, 2011.

Sun, B., Li, C. Y., Cordovil, C. M. D. S., Jia, K. L., Zhang, S., de Varennes, A., and Pereira, L. S.: Variability of water quality in Ulansuhai Lake receiving drainage water from Hetao Irrigation system in Yellow River Basin, China, Fresen. Environ. Bull., 22, 1666–1676, 2013.

Verpoorter, C., Kutser, T., Seekell, D. A., and Tranvik, L. J.: A global inventory of lakes based on high-resolution satellite imagery, Geophys. Res. Lett., 41, 6396–6402, 2014.

Volkov, S., Bogdaonv, S., Zdorovennov, R., Zdorovennova, G., Terzhevik, A., Palshin, N., Bouffard, D., and Kirillin, G.: Fine scale structure of convective mixed layer in ice-covered lake, Environ. Fluid Mech., 19, 751–764, 2019.

Wang, B., Ma, Y., Chen, X., Ma, W., Su, Z., and Menenti, M.: Observation and simulation of lake-air heat and water transfer processes in a high-altitude shallow lake on the Tibetan Plateau, J. Geophys. Res.-Atmos., 120, 12327–12344, 2015.

Winters, K. B., Ulloa, H. N., Wüest, A., and Bouffard, D.: Energetics of radiatively heated ice-covered lakes, Geohpys. Res. Lett., 45, 8913–8925, 2019.

Yang, B., Wells, M. G., McMeans, B. Dugan, H. A., Rusak, J. A., Weyhenmeyer, G. A.,Brentrup, J. A., Hrycik, A. R., Laas, A., Pilla, R. M., Austin, J. A., Blaunchfield, P. J., Carey, C. C., Guzzo, M. M., Lottig, N. R., Mackay, M. D., Middel, T. A., Pierson, D. C., Wang, J., and Young, J. D.: A new thermal categorization of ice-covered lakes, Geophys. Res. Lett., 48, e2020GL091374, https://doi.org/10.1029/2020GL091374, 2020.

Yang, F., Cen, R., Feng, W., Zhu, Q., Leppäranta, M., Yang, Y., Wang, X., and Liao, H.: Dynamic simulation of nutrient distribution in lakes during ice cover growth and ablation, Chemosphere, 281, 130781, https://doi.org/10.1016/j.chemosphere.2021.130781, 2021.

Yang, F., Li, C., Leppäranta, M., Shi, X., Zhao, S., and Zhang, C.: Notable increases in nutrient concentrations in a shallow lake during seasonal ice growth, Water Sci. Technol., 74, 2773–2883, 2016.

Zhu, D. N., Cathryn, R. M., Sun, B., and Li, C. Y.: The influence of irrigation and Ulansuhai Lake on groundwater quality in eastern Hetao Basin, Inner Mongolia, China, Hydrogeol. J., 22, 1101–1114, 2014.